


# Magnetization Dynamics Induced by Nanoconfined Magnetic-Field Pulse Generated by Resonant Plasmonic Nanoantennas

B.C. Choi\*

*Department of Physics and Astronomy, University of Victoria, Victoria V8P 5C2, Canada*

 (Received 16 January 2019; revised manuscript received 14 March 2019; published 10 April 2019)

Finite-difference time domain (FDTD) calculations reveal that resonant plasmonic nanoantennas are capable of generating intense magnetic field pulses in the midinfrared frequency region. The magnetic field pulse generated by nanoantennas is spatially concentrated within a nanoscale region, with its intensity increased by more than two orders of magnitude compared to that of the incident light. Given the highly localized confinement of the intense magnetic field, the nanoantenna can be used as a nanoscale source of magnetic field pulse at optical frequencies, which can locally manipulate the magnetism within a very short time scale. Micromagnetic numerical results demonstrate the excitation of the magnetization oscillation in a ferromagnetic nanoelement, which is coherently coupled to the magnetic field. After the termination of magnetization oscillation, propagating spin waves emerge from the excitation magnetic field region and travel perpendicular to the static magnetization direction. The result demonstrates the potential of resonant plasmonic nanoantennas in optically triggering magnetization dynamics and subsequently generating spin waves in the GHz frequency domain. The result opens up an interesting perspective for applying plasmonic nanoantennas in the ultrafast optical manipulation of magnetism on the nanometer scale.

DOI: [10.1103/PhysRevApplied.11.044028](https://doi.org/10.1103/PhysRevApplied.11.044028)

## I. INTRODUCTION

The study of nonequilibrium magnetization phenomena in magnetic elements has attracted much attention due to the fundamental interest in ultrafast magnetization dynamics and a variety of potential applications, including high-speed magnetoelectronic devices. Conventionally, the magnetization dynamics in magnetic elements have been triggered by applying magnetic field pulses or spin torque [1,2]. With the latest advances in laser technology, the possibility of the optical excitation of magnetism by employing high-power lasers has been extensively explored. In their pioneering work of laser-induced ultrafast demagnetization, Beuerepaire *et al.* demonstrated that ferromagnetic (FM) thin films excited by femtosecond laser pulses underwent ultrafast demagnetization within several hundred femtoseconds due to rapid energy transfer from thermalized electrons to the spin system [3]. The demagnetization was followed by a slow recovery over the picosecond timescale as electrons equilibrate with the phonons, and eventually to complete cooling via nanosecond lattice diffusion. The timescale of the laser-induced demagnetization process is orders of magnitude below the limit imposed by conventional switching of magnetic order via magnetic field pulse, and has been the focus of considerable research since its discovery. The laser-induced ultrafast magnetization process is, however, incoherent in

nature, and it has been challenging to coherently control magnetic states.

Over the past years, significant research efforts have been devoted to exploring new phenomena in the interaction of light with magnetism. Recently, an increasing number of THz magnetization dynamics studies have emerged in which the magnetic field component of optical pulses directly couples to the magnetization via Zeeman coupling [4]. Kampfrath *et al.*, for example, reported on the coherent control of spin waves in antiferromagnetic NiO with highly intense terahertz pulses [5]. Recent work by Shalaby *et al.* also demonstrated the magnetization dynamics in ferromagnets triggered by intense THz magnetic pulses, and found that the excited magnetization oscillation was phase locked to the magnetic field [6]. Another rapidly emerging field of research is magneto-plasmonics, which combines both magnetic and plasmonic functionalities [7]. Of particular relevance to information technology is that the incorporation of plasmonic nanostructures to magnetic systems can lead to a significant enhancement of the magneto-optical (MO) response. Recently, V. Bonanni *et al.* reported the magneto-plasmonic effect in FM nanostructures, in which a strong and tunable correlation between the localized surface plasmons and magneto-optical effect was observed [8].

In this study, we explore an alternative venue for optically manipulating magnetism by directly applying a nanoconfined magnetic field pulse generated by plasmonic nanoelements. Plasmonic nanostructures, such as split-ring

\*bchoi@uvic.ca

resonators [9–11], dielectric dimers [12], and nanoantennas [13–16], have been widely studied due to their capabilities to convert optical radiation to intense magnetic fields. In particular, T. Grosjean *et al.* introduced an alternative nanoantenna concept, which was based on the diabolo nanostructure and could generate significantly enhanced magnetic field in the optical frequency range [14]. In our numerical study, the intense magnetic field pulses in the midinfrared frequency region are generated by employing plasmonic diabolo nanoantennas. The strongly confined magnetic field is used to focus intense magnetic field pulses on a FM nanowire to excite magnetization dynamics. It is found that the local perturbation of the magnetic order induced by the direct coupling between the magnetization and nanoconfined magnetic field pulses leads to the emission of propagating spin waves.

## II. PLASMONIC NANOANTENNA FOR OPTICAL MAGNETIC FIELD ENHANCEMENT

The properties of a plasmonic nanoantenna combined with FM thin films are studied using finite-difference time domain (FDTD) simulations, in which Maxwell's equations are numerically solved by iteration over time [17]. The hybrid plasmonic-FM structure consists of a pair of Ag nanoantennas, SiO<sub>2</sub> spacer layers, and FM thin film. In the modeling, a 10-nm thick Ni film is used as the magnetic medium since the optical effect in nickel-rich Permalloy is very similar to that in Ni in the visible and near-infrared regions [18]. The dielectric permittivity values of Ni are taken from Johnson and Christy data [19]. As shown in the schematic in Fig. 1(a), the nanoantenna is based on the diabolo structure, which is a pair of metallic triangular nanostructures connected by a junction [16]. The bottom nanoantenna is embedded in a SiO<sub>2</sub> substrate, whereas the top counterpart is surrounded by air. The geometry of

the nanoantenna is  $240 \times 240 \times 100 \text{ nm}^3$ , with the junction of  $50 \times 50 \times 100 \text{ nm}^3$ . The 10-nm thick Ni layer is placed between nanoantennas in which the 5-nm SiO<sub>2</sub> spacer layers electrically insulate the Ni layer from the Ag antennas. The maximum magnetic field achievable for the given geometry of nanoantenna is optimized by varying the SiO<sub>2</sub> spacer layer thickness at a fixed Ni thickness of 10 nm. The nanoantennas are illuminated with a plane wave propagating downward along the  $-z$  direction with its electric field linearly polarized along the  $y$  direction. At resonance, free electrons in the metallic nanoantennas are collectively excited by the electric field of the incident light, and, consequently, a highly localized magnetic field is generated by the electrical current flowing through the junction. Figure 1(b) shows the spectral response of the normalized magnetic field intensity  $|B_R|^2/|B_o|^2$ .  $B_R$  corresponds to the magnetic field at resonance generated inside the magnetic medium between the nanoantenna junction, whereas  $B_o$  is the magnetic field of the incident light. It is found that the nanoantennas support a strong magnetic resonance, which occurs in the infrared regime with a central wavelength of  $2.74 \mu\text{m}$ . At the magnetic resonance, the magnetic field intensity is enhanced by more than two orders of magnitude compared to that of the incident light.

Figure 2(a) illustrates the spatial distribution of the normalized magnetic field intensity,  $|B_R|^2/|B_o|^2$ , calculated inside the magnetic medium under the magnetic resonance condition. A magnetic hotspot, where the intense magnetic field is spatially concentrated, is generated between nanoantenna junctions. This strong confinement provides an opportunity to focus intense magnetic fields into a small region while overcoming the restriction of the diffraction limit defined by the Rayleigh criterion in optical excitations. Figure 2(b) represents the time trace of the normalized magnetic field  $B_R$  as compared to the optical magnetic field component  $B_o$  of the incident light. It reveals the

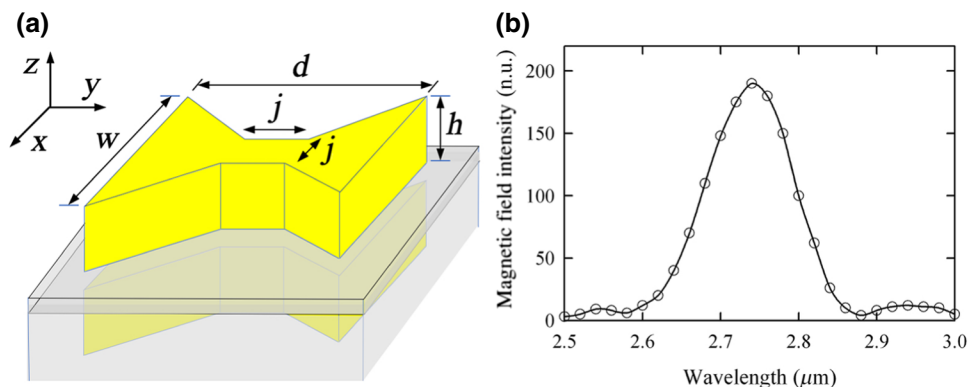


FIG. 1. (a) Schematic diagram of a sandwich diabolo nanoantenna with  $w = 240 \text{ nm}$ ,  $d = 240 \text{ nm}$ ,  $h = 100 \text{ nm}$ , and  $j = 50 \text{ nm}$ . The layer between diabolo nanostructures is composed of SiO<sub>2</sub> (5 nm)/Ni (10 nm)/SiO<sub>2</sub> (5 nm). A plane wave is incident from the top with its electric field  $E$  along the  $y$  direction. The magnetic field is generated in the junction along the  $x$  direction. (b) Spectral response of the normalized magnetic field intensity  $|B_R|^2/|B_o|^2$  as a function of the wavelength of incident light. The intensity is calculated inside the magnetic medium between the junctions. The magnetic resonance occurs in the infrared regime, centered at  $2.74 \mu\text{m}$ .

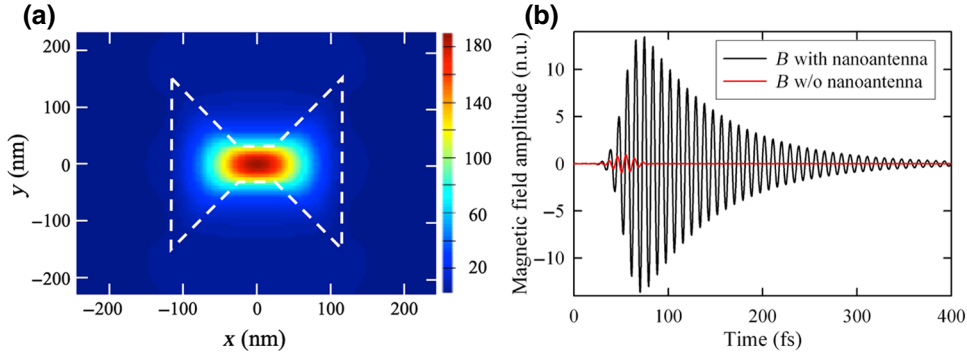


FIG. 2. (a) Spatial distribution of the normalized magnetic field intensity,  $|B_R|^2/|B_o|^2$ , in the  $xy$  plane inside the magnetic medium. The position of the diablo nanoantenna is indicated by the dotted line. Intense magnetic field is spatially concentrated between nanoantenna junctions. (b) Temporal profile of the normalized magnetic field,  $B_R/B_o$ , at resonance. Red curve represents the optical magnetic field component  $B_o$  of the incident light.

characteristic of damped harmonic oscillator with the frequency of 108 THz, and its peak magnetic field is increased more than 12 times compared to the optical magnetic field of the incident light (shown as red). It is noteworthy that the duration of the induced magnetic field  $B_R$  is significantly longer compared to that of the incident field  $B_o$ . This is an intrinsic property of the plasmonic resonator, in which the electric current continues to oscillate in the junction even after the termination of the incident light. This resonating behavior of the plasmonic nanoantenna provides both the magnetic field enhancement and the elongation of the magnetic pulse duration. Given the strong confinement of the intense magnetic field, the nanoantenna can be used as a nanoscale-sized source of magnetic fields, which can locally manipulate the magnetism on ultrashort time scales. In order to explore this potential, the dynamic properties of FM nanoelements in response to the application of a locally confined magnetic field is numerically investigated.

### III. MAGNETIZATION EXCITATION BY NANOCONFINED MAGNETIC FIELD PULSE

The ultrafast manipulation of the magnetization with magnetic fields and its effect on the magnetization dynamics on a longer time scale are studied using micromagnetic finite-element modeling based on the Landau–Lifshitz–Gilbert equation [20,21]

$$dM/dt = -|\gamma/(1 + \alpha^2)|(M \times B_{\text{eff}}) - |(\alpha\gamma)/[M_S(1 + \alpha^2)]| \times [M \times (M \times B_{\text{eff}})].$$

Here,  $\gamma$  is the gyromagnetic ratio and  $\alpha$  is a phenomenological damping constant.  $B_{\text{eff}}$  is the total effective field acting on the magnetization  $M$ , which mainly includes the applied external field, the exchange interaction, and the demagnetizing field. In modeling, a 10-nm thick Permalloy ( $\text{Ni}_{80}\text{Fe}_{20}$ ) waveguide with lateral dimensions

of  $120 \text{ nm} \times 4 \text{ }\mu\text{m}$  is subdivided into homogeneously magnetized unit cells of the dimension  $5 \times 5 \times 5 \text{ nm}^3$ . The unit cell size is comparable to the exchange length of Permalloy [22]. The material parameters used in the modeling are: saturation magnetization ( $M_S = 800 \text{ emu/cm}^3$ ), exchange stiffness ( $A = 1.05 \times 10^{-6} \text{ ergs/cm}$ ), and damping constant ( $\alpha = 0.008$ ). The modeling is carried out at 0 K. A damping boundary condition, in which the damping constant is gradually increased at both ends of the waveguide, is applied in order to suppress the reflection of spin waves [23]. A uniform bias magnetic field of 400 mT is applied along the  $y$  direction so that the magnetization in the waveguide is aligned perpendicular to the long axis of the magnetic element. In order to excite the magnetization, the temporally varying magnetic field  $B_R$ , which has the same temporal profile as that in Fig. 2(b), is applied along the  $x$  direction in the middle of the waveguide. In order to model the nanoconfinement of  $B_R$ , the magnetic field is focused within the area of  $120 \times 60 \text{ nm}^2$  in the middle section of the magnetic waveguide. The position of the localized  $B_R$  region is marked with a dashed box, as shown in the inset of Fig. 3(b).  $B_R$  is assumed to be uniform throughout the thickness of the magnetic film within the area. The peak magnetic field of 50 mT is used in the modeling, which is experimentally achievable by employing diablo nanoantennas with laser fluence as low as  $0.1 \text{ mJ/cm}^2$ . From a practical application point of view, it is important to control the plasmonic enhanced electric field and heat generation in nanodevices under critical limits in order to avoid an extreme influence of electromigration and heat dissipation from the metallic element to the adjacent  $\text{SiO}_2$  and FM layers [24]. FDTD calculation confirms a considerable electric field enhancement, mainly at the end sides of the nanoantenna elements, up to 8.8 MV/m with a fluence of  $0.1 \text{ mJ/cm}^2$ . This enhanced electric field, however, is much smaller compared to the previously reported field of 100 GV/m, which was estimated in a tunneling gap with dimensions of a few nanometers and did not cause

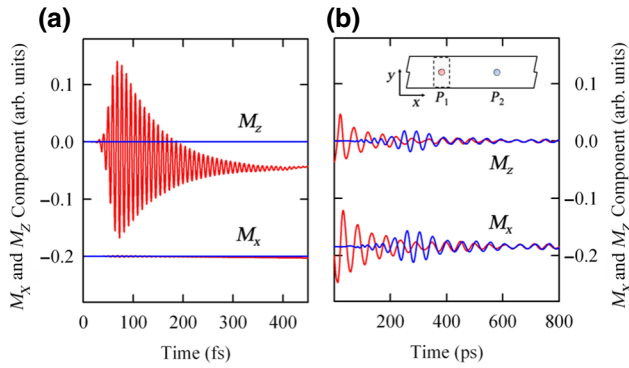


FIG. 3. Temporal responses of out-of-plane magnetization components  $M_z(t)$  and in-plane components  $M_x(t)$  for the time intervals: (a) from 0 to 450 fs and (b) from 1 to 800 ps. A magnetic field pulse is applied along the  $x$  direction at  $t = 0$  fs. Curves are vertically shifted for comparison. (*inset*) Dashed box marks the position of the localized magnetic near field region, while the probing areas  $P_1$  and  $P_2$  are represented with dotted circles with diameters of 20 nm.  $P_2$  is located 200 nm away from the center of  $P_1$ . Red and blue curves in (a) and (b) correspond to the local magnetic responses averaged over the areas  $P_1$  and  $P_2$ , respectively.

damage of nanodevices [25]. The plasmonic enhancement of temperature in nanostructures is also calculated using the general expression of heat generation [26]. The calculation with the fluence value of  $0.1 \text{ mJ/cm}^2$  predicts a maximum temperature of 1030 K at electric hotspots, which is well below the melting temperature of 1235 K for Ag. The conductive heat transfer from Ag nanoantennas to  $\text{SiO}_2$  and FM layers is investigated using the finite-element analysis modeling software COMSOL MULTIPHYSICS [27]. The resulting temperature distribution indicates that the temperature increase in the magnetic layer is negligible due to the low thermal conductivity of the  $\text{SiO}_2$  layer [28].

Figure 3(a) shows the dynamic responses of the local magnetization  $M_x(t)$  and  $M_z(t)$  for the first 450 fs after applying  $B_R$  at time  $t = 0$  fs. The response of the magnetization is spatially averaged over the areas with a diameter of 20 nm, which are located at  $P_1$ , that is, within the excitation field region, and at  $P_2$ , that is, 200 nm away from the center of  $P_1$  along the long axis of the waveguide, respectively. An important observation is the drastic difference in the dynamic response between the components  $M_x$  and  $M_z$  measured over  $P_1$ , in which the out-of-plane magnetization component  $M_z$  exhibits a large change whereas the response of the in-plane component  $M_x$  is insignificant. The change of the  $M_y$  component is also very small and is not shown. The dominance of the  $M_z$  component in the magnetization dynamics is attributed to the field configuration of  $\mathbf{M} \perp \mathbf{B}_R$ , in which the magnetization vector  $\mathbf{M}$  experiences the Zeeman torque ( $\mathbf{M} \times \mathbf{B}_R$ ) that leads to a significant out-of-plane magnetization contribution to the dynamics. A distinct feature found in  $M_z(t)$  is that the

magnetization oscillation with the frequency of approximately 100 THz is directly coupled to the driving magnetic field. The magnetization oscillates coherently with  $\mathbf{B}_R$ , and the oscillation amplitude decays with decreasing field amplitude of  $\mathbf{B}_R$ . This result is in a qualitative agreement with the previous report by Shalaby *et al.* in which a THz-induced coherent oscillation of the magnetization in 15-nm thick Co film was observed [29]. The direct coupling of the magnetization dynamics with  $\mathbf{B}_R$  is further corroborated by comparing the magnetic response averaged over the probing area  $P_2$ , which is located outside the spatially confined magnetic field. As expected, no measurable magnetic response is found outside the  $\mathbf{B}_R$  region due to the absence of the Zeeman torque.

Interesting features of the magnetization dynamics appear after the near complete relaxation of the  $\mathbf{B}_R$  field-driven coherent magnetization oscillation. Figure 3(b) shows the temporal changes of  $M_x$  and  $M_z$  components, averaged over  $P_1$  and  $P_2$ , for longer time scales  $t > 1$  ps. In contrast to the  $\mathbf{B}_R$  field-induced magnetization dynamics shown in Fig. 3(a), dynamic components of the magnetization appear not only within the  $\mathbf{B}_R$  excitation region, but also in the adjacent region. Moreover, oscillatory behaviors become noticeable in both the  $M_x$  and  $M_z$  components. This implies that the  $\mathbf{B}_R$ -induced perturbation in the magnetic order within the  $P_1$  region acts as the source of the delayed magnetic response in the form of magnetization precession in the vicinity of the excitation field region. From a microscopic point of view, the observation of the magnetization precession outside the  $\mathbf{B}_R$  field region can be interpreted to be the result of the excitation of propagating spin waves, in which the waves travel perpendicular to the direction of the static magnetization. The spin waves excited in this static magnetization-magnetic field configuration correspond to the Damon-Eshbach (DE) mode [30]. The spin wave excitation is attributed to the rapid relaxational process of the magnetization dynamics from  $\mathbf{B}_R$ -induced nonequilibrium state, in which the excess of magnetic energy is transformed into spin waves. In general, the magnetization relaxation from magnetic nonequilibrium is accompanied by the change of the energy in the magnetic system. It was discussed by Suhl and Safonov that the energy released during relaxation can be accommodated by spin waves [31,32]. Since the modulation of spin waves is mediated by the short-range exchange interaction of precessing magnetic moments, the characteristic time of such a modulation is given by the precessional frequency, which is typically in the range of a few gigahertz in FM materials [33].

Further insight into the details of propagating spin waves can be obtained by analyzing the spatially dependent dynamic components of the magnetization. Figure 4(a) shows the temporal scans of the  $M_x$  component averaged over the areas of 20 nm in diameter at various distances from the  $\mathbf{B}_R$  excitation region. The probing



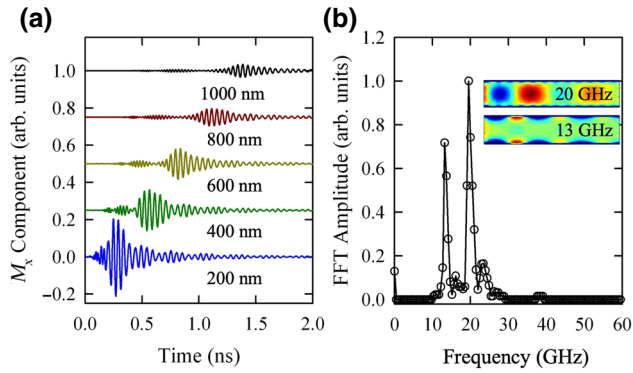


FIG. 4. (a) Temporal properties of spin waves measured at various probing positions along the long axis of the waveguide. Numbers indicate the distance between  $B_R$  excitation and probing regions. A burst of spin waves is launched from the excitation region and propagates along the waveguide. Curves are vertically shifted for comparison. (b) Frequency spectrum reveals a main peak corresponding to the spin wave mode at 20 GHz. The peak at 13 GHz is associated with the spin wave mode propagating along the waveguide edge. (Inset) The FFT amplitude distributions are shown for the frequencies of 13 and 20 GHz, respectively.

positions are equidistantly separated by 200 nm along the long axis of the waveguide. At the probing position at a distance of 200 nm from the center of the  $B_R$  excitation region, one observes that a burst of spin waves is emitted from the excitation field region and travels away with time. The propagating spin waves lead to the formation of a spin wave packet. The amplitude of spin waves gradually decreases due to the intrinsic damping of the magnetic medium. The spin wave velocity of approximately 1 km/s is estimated from the time delay of the shift of the wave packets probed at different positions. One also observes the formation of the higher-frequency wave packets with very small amplitudes, which can be clearly seen at the positions of 400 and 600 nm. The propagation velocity of these high-frequency spin waves is slightly higher and estimated at approximately 1.2 km/s. These values are in the comparable range as those previously reported spin wave velocities measured in Permalloy microstrips [34]. Figure 4(b) is the result of the fast Fourier transform (FFT) analysis of the data shown in Fig. 4(a). The frequency spectrum reveals a predominant peak at approximately 20 GHz, which corresponds to the major spin wave mode. The images shown in the inset of Fig. 4(b) are the FFT amplitude distributions captured at frequencies of 13 and 20 GHz, respectively. The spin waves at 20 GHz are strongly focused in the middle region of the waveguide. In contrast, the spin wave mode at 13 GHz is localized along the edges. The 13-GHz mode is associated with the spin waves propagating along the waveguide edge, which is attributed to the presence of the narrow waveguiding channels induced by the edge potential wells due to the nonuniform distribution of the internal static magnetic field

near the edges [35]. The excitation of such an edge mode in submicrometer magnonic waveguides has been previously observed by Xing *et al.* [36].

#### IV. CONCLUSIONS

We demonstrate that plasmonic nanoantennas are capable of generating intense magnetic fields in the mid-IR region. Since the magnetic fields are highly confined, they are ideally suited as nanoscale-sized sources of magnetic fields, which can effectively manipulate the magnetism within a very short time scale. Micromagnetic numerical results demonstrate the coherent oscillation of the magnetization upon excitation by nanoconfined magnetic fields, which is followed by the emission of propagating spin waves with a few GHz frequencies. Considering the significant current challenges of effectively coupling spins in nanoscale magnetic elements to the magnetic component of the electromagnetic fields, the result offers the strong potential of plasmonic nanoantennas in the application of spintronics.

#### ACKNOWLEDGMENTS

The author acknowledges funding from the NSERC (Canada) Discovery Grants program. It is a pleasure to acknowledge fruitful discussions with Professor Reuven Gordon.

- [1] M. Freeman and B. C. Choi, Advances in magnetic microscopy, *Science* **294**, 1484 (2001).
- [2] J. C. Slonczewski, Current-driven excitation of magnetic multilayers, *J. Magn. Magn. Mater.* **159**, L1 (1996).
- [3] E. Beurepaire, J. Merle, A. Daunois, and J. Bigot, Ultrafast Spin Dynamics in Ferromagnetic Nickel, *Phys. Rev. Lett.* **76**, 4250 (1996).
- [4] S. Wienholdt, D. Hinzke, and U. Nowak, THz Switching of Antiferromagnets and Ferrimagnets, *Phys. Rev. Lett.* **108**, 247207 (2012).
- [5] T. Kampfrath, A. Sell, G. Klatt, O. Pashkin, S. Mährlein, T. Dekorsy, M. Wolf, M. Fiebig, A. Leitenstorfer, and R. Huber, Coherent terahertz control of antiferromagnetic spin waves, *Nat. Photonics* **5**, 31 (2010).
- [6] M. Shalaby, A. Donges, K. Carva, R. Allenspach, P. Oppeneer, U. Nowak, and C. Hauri, Coherent and incoherent ultrafast magnetization dynamics in 3dferromagnets driven by extreme terahertz fields, *Phys. Rev. B* **98**, 014405 (2018).
- [7] G. Armelles and A. Dmitrev, Focus on magnetoplasmonics, *New J. Phys.* **16**, 045012 (2014).
- [8] V. Bonanni, S. Bonetti, T. Pakizeh, Z. Pirzadeh, J. Chen, J. Nogués, P. Vavassori, R. Hillenbrand, J. Åkerman, and A. Dmitriev, Designer Magnetoplasmonics with Nickel Nanoferrromagnets, *Nano Lett.* **11**, 5333 (2011).

- [9] H. Y. Feng, F. Luo, L. Henrad, F. Garcia, G. Armelles, and A. Cebollada, Active magnetoplasmonic split-ring/ring nanoantennas, *Nanoscale* **9**, 37 (2017).
- [10] Y. Yang, H. T. Dai, and X. W. Sun, Split ring aperture for optical magnetic field enhancement by radially polarized beam, *Opt. Express* **21**, 6845 (2013).
- [11] J. Zhou, T. Koschny, M. Kafesaki, E. Economou, J. Pendry, and C. Soukoulis, Saturation of the Magnetic Response of Split-Ring Resonators at Optical Frequencies, *Phys. Rev. Lett.* **95**, 223902 (2005).
- [12] P. Albella, M. Poyli, M. Schmidt, S. Maier, F. Moreno, J. Sanez, and J. Aizpurua, Low-loss electric and magnetic field-enhanced spectroscopy with subwavelength silicon dimers, *J. Phys. Chem. C* **117**, 13573 (2013).
- [13] V. Giannini, A. I. Fernández-Domínguez, S. C. Heck, and S. A. Maier, Plasmonic nanoantennas: Fundamentals and their use in controlling the radiative properties of nanoemitters, *Chem. Rev.* **111**, 3888 (2011).
- [14] T. Grosjean, M. Mivelle, F. I. Baida, G. W. Burr, and U. C. Fischer, Diabolo nanoantenna for enhancing and confining the magnetic optical field, *Nano Lett.* **11**, 1009 (2011).
- [15] P. Muhlschlegel, H. Eisler, O. Martin, B. Hecht, and D. Pohl, Resonant optical antennas, *Science* **308**, 1607 (2005).
- [16] M. Mivelle, T. Grosjean, G. Burr, U. Fischer, and M. Garcia-Parajo, Strong modification of magnetic dipole emission through diabolo nanoantennas, *ACS Photonics* **2**, 1071 (2015).
- [17] Lumerical Solutions, [www.lumerical.com](http://www.lumerical.com)
- [18] T. Yoshino and S. Tanaka, Longitudinal magneto-optical effect in Ni and nickel-rich Ni-Fe films in visible and near infrared regions, *Opt. Commun.* **1**, 149 (1969).
- [19] P. Johnson and R. Christy, Optical constants of the noble metals, *Phys. Rev. B* **6**, 4370 (1972).
- [20] Q. F. Xiao, J. Rudge, B. C. Choi, Y. K. Hong, and G. Donohoe, Dynamics of ultrafast magnetization reversal in submicron elliptical Permalloy thin film elements, *Phys. Rev. B* **73**, 104425 (2006).
- [21] LLG Micromagnetic Simulator, [www.llgmicro.mindspring.com](http://www.llgmicro.mindspring.com)
- [22] G. Abo, Y. Hong, J. Park, J. Lee, W. Lee, and B. Choi, Definition of magnetic exchange length, *IEEE Trans. Magn.* **49**, 4937 (2013).
- [23] S. Bance, T. Schrefl, G. Hrkac, A. Goncharov, D. Allwood, and J. Dean, Micromagnetic calculation of spin wave propagation for magnetologic devices, *J. Appl. Phys.* **103**, 07E735 (2008).
- [24] M. Brongersma, N. Halas, and P. Nordlander, Plasmon-induced hot carrier science and technology, *Nat. Nanotechnol.* **10**, 25 (2015).
- [25] T. Rybka, M. Ludwig, M. Schmalz, V. Knittel, D. Brida, and A. Leitenstorfer, Sub-cycle optical phase control of nanotunnelling in the single-electron regime, *Nat. Photonics* **10**, 667 (2016).
- [26] G. Baffou, R. Quidant, and C. Girard, Heat generation in plasmonic nanostructures: Influence of morphology, *Appl. Phys. Lett.* **94**, 153109 (2009).
- [27] COMSOL Multiphysics® Modeling Software, [www.comsol.com](http://www.comsol.com)
- [28] See Supplemental Material at <http://link.aps.org/supplemental/10.1103/PhysRevApplied.11.044028> for details of the heat transfer modeling.
- [29] M. Shalaby, C. Vicario, and C. Hauri, Low frequency terahertz-induced demagnetization in ferromagnetic nickel, *Appl. Phys. Lett.* **108**, 182903 (2016).
- [30] R. W. Damon and J. R. Eshbach, Surface magnetostatic modes and surface spin waves, *Phys. Rev.* **118**, 5 (1960).
- [31] H. Suhl, Theory of the magnetic damping constant, *IEEE Trans. Magn.* **34**, 1834 (1998).
- [32] V. L. Safonov and H. N. Bertram, Spin-wave dynamic magnetization reversal in a quasi-single-domain magnetic grain, *Phys. Rev. B* **63**, 094419 (2001).
- [33] R. Arias and D. L. Mills, Extrinsic contributions to the ferromagnetic resonance response of ultrathin films, *Phys. Rev. B* **60**, 7395 (1999).
- [34] P. Wessels, A. Vogel, J.-N. Tödt, M. Wieland, G. Meier, and M. Drescher, Direct observation of isolated Damon-Eshbach and backward volume spin-wave packets in ferromagnetic microstripes, *Sci. Rep.* **6**, 22117 (2016).
- [35] V. Demidov, S. Demokritov, K. Rott, P. Krzysteczko, and G. Reiss, Nano-optics with spin waves at microwave frequencies, *Appl. Phys. Lett.* **92**, 232503 (2008).
- [36] X. Xing, S. Li, X. Huang, and Z. Wang, Current-controlled unidirectional edge-meron motion, *AIP Adv.* **3**, 032144 (2013).